Effect of temperature on domain wall–pore interactions in lead zirconate titanate: A phase-field study

Author(s):
Indergand, Roman; Kochmann, Dennis M.

Publication date:
2021-11-29

Permanent link:
https://doi.org/https://doi.org/10.3929/ethz-b-000518695

Originally published in:
Applied Physics Letters 119(22), https://doi.org/10.1063/5.0066612

Applied Physics Letters ARTICLE scitation.org/journal/apl

Effect of temperature on domain wall–pore interactions in lead zirconate titanate: A phase-field study

Cite as: Appl. Phys. Lett. **119**, 222901 (2021); doi: 10.1063/5.0066612
Submitted: 11 August 2021 · Accepted: 12 November 2021 ·
Published Online: 2 December 2021

R. Indergand and D. M. Kochmann[a)]

AFFILIATIONS

Mechanics & Materials Lab, Department of Mechanical and Process Engineering, ETH Zürich, 8092 Zürich, Switzerland

[a)]Author to whom correspondence should be addressed: dmk@ethz.ch

ABSTRACT

We study the influence of temperature on the interaction of nano-pores with ferroelectric domain walls in bulk single-crystalline lead zirconate titanate as a function of pore size and concentration. Using a density functional theory-informed finite-temperature phase-field model, we determine the electric field required to unpin 180°-domain walls from a periodic array of pores, thus gaining insight into the effect of temperature on domain wall kinetics in ferroelectrics with good qualitative agreement between simulated results and experimental measurements.

Ferroelectric materials have a permanent electric dipole moment (or spontaneous polarization) which can be altered by electric fields. This unique property—in combination with their electro-mechanical,[1] thermoelectric,[2] and electro-optical coupling[3]—makes ferroelectrics a versatile class of materials for, e.g., transducers, actuators, sensors, and memory devices. Since the effective kinetics of polarization switching at the macroscale is strongly determined by the collective motion[4,5] of individual domain walls (DWs) at smaller scales,[6–8] understanding the underlying physics of DW motion and its interaction with defects in realistic materials (which typically show high sintering-induced porosity with nano- to micrometer-sized pores[9]) is key for accurate predictions of microstructure-property relations.

Pores can introduce substantial local mechanical[10–12] and electric fields[11–13] in their vicinity which interfere with DW motion, thus influencing the ferroelectric and piezoelectric properties[14] in bulk[14,15] and thin films.[11] For instance, recent studies on (an-)isometric pores investigated the effect of pore concentration, size, anisotropy, and orientation for tuning the piezoelectric properties of lead zirconate titanate[15–17] (PZT). Experiments have demonstrated the effects of DW pinning across scales: At the macroscale, the influence of dopants, oxygen vacancies, and crystal structures in PZT on the bipolar hysteresis behavior was investigated,[18–20] while insight into the microscopic kinetics of polarization reversal was gained by tracking individual DWs via atomic force microscopy, piezoresponse force microscopy, and polarization sensitive collection mode near-field scanning optical microscopy.[21–25]

When modeling DW motion in complex geometries at realistic scales, phase-field techniques are often the method of choice to predict material behavior. Various types of defects have been studied by phase-field models: from space charges and oxygen vacancy migration at the atomic level[26] over impurities, voids,[27] dislocations,[28] and grain boundaries[29] at the mesoscale to cracks,[30] notches, and free surfaces[31] at the macroscopic device level. At larger scales, scaling arguments and functional renormalization group techniques have been used to study DW pinning in disordered elastic systems for random bond and field disorder,[32,33] crystal-lattice and disorder pinning,[34,35] and the dipolar interaction of incommensurate–commensurate transitions.[36] Stemming from nonlinear continuum mechanics, a theory for interface motion in homogeneous[37–40] and heterogeneous materials[41,42] was established and used to study, among others, the role of the defect length scale on the pinning of interface motion as well as the influence of grain boundary, size, and triple junctions,[43,44] and its impact on the macroscopic hysteresis.

Although various models have, thus, been proposed to study the influence of pores, the effect of temperature on DW (de-)pinning is insufficiently considered in general but plays an important role on DW kinetics, as evident from experiments.[25,45,46] We, therefore, use a finite-temperature phase-field framework,[47] which—calibrated by

Density Functional Theory (DFT) data—captures the temperature dependence of the Ginzburg–Landau energy as well as thermal fluctuations. This allows us to gain insight into the effect of temperature on pore–DW interactions for an enhanced predictability of the kinetics of ferroelectric materials, and more generally, it provides an efficient numerical tool to probe the temperature-dependent influence of microstructural features.

As the length and time scales of interest lie outside the realm of first-principles techniques, we use a phase-field description based on the well-established Devonshire–Ginzburg–Landau theory[48,49] with the total polarization vector $\boldsymbol{p}$ as the order parameter, describing the evolution of the ferroelectric microstructure by resolving the diffuse interfaces between ferroelectric domains. We simulate a Representative Volume Element (RVE) of a ferroelectric material, whose electromechanical response is described by the mechanical displacement field $\boldsymbol{u}(\boldsymbol{x}, t)$ and electric potential $\phi(\boldsymbol{x}, t)$, both dependent on position $\boldsymbol{x}$ and time t. The mechanical problem is governed by the balance of linear momentum (in the absence of body forces and inertial effects),

$$\nabla \cdot \boldsymbol{\sigma} = 0, \tag{1}$$

where $\boldsymbol{\sigma}$ is the Cauchy stress tensor. The electrical problem obeys Gauss' law (assuming no free charges),

$$\nabla \cdot \boldsymbol{d} = 0, \quad \text{where} \quad \boldsymbol{d} = \kappa_0 \boldsymbol{e} + \boldsymbol{p} \tag{2}$$

is the electric displacement field linked to the electric field $\boldsymbol{e} = -\nabla\phi$ through the permittivity of free space, κ_0. We assume a uniform temperature θ within the material, whose electric enthalpy density is of the form[50,51]

$$\begin{aligned} W(\boldsymbol{\varepsilon}, \boldsymbol{e}, \boldsymbol{p}, \nabla\boldsymbol{p}, \theta) = {} & \Psi_{\text{mech.}}(\boldsymbol{\varepsilon}) + \Psi_{\text{coupl.}}(\mathbf{eps}, \mathbf{p}) + \Psi_{\text{pol.}}(\boldsymbol{p}, \theta) \\ & + \Psi_{\text{el.}}(\boldsymbol{e}) + \Psi_{\text{inter.}}(\nabla\boldsymbol{p}) - \boldsymbol{e} \cdot \boldsymbol{p}, \end{aligned} \tag{3}$$

comprising the mechanical energy density $\Psi_{\text{mech.}}$ dependent on strain tensor $\boldsymbol{\varepsilon} = \frac{1}{2}(\nabla\boldsymbol{u} + \nabla\boldsymbol{u}^\top)$, coupling energy density $\Psi_{\text{coupl.}}$, polarization (Landau) potential $\Psi_{\text{pol.}}$ as well as electric and interface energy densities $\Psi_{\text{el.}}$ and $\Psi_{\text{inter.}}$, respectively. Material constants (which have been adapted from DFT calculations for tetragonal PZT[52]) and the specific form of the above energy densities are summarized in the supplementary material, Sec. I. Constitutive relations follow as $\boldsymbol{\sigma} = \partial W/\partial\boldsymbol{\varepsilon}$ and $\boldsymbol{d} = -\partial W/\partial\boldsymbol{e}$. The polarization potential $\Psi_{\text{pol}}(p, \theta)$—and hence its minimizer, the spontaneous polarization p_0—is temperature-dependent. Below the Curie temperature θ_{C} (for PZT $\theta_{\text{C}} = 650$ K), from minimizing $\Psi_{\text{pol.}}(\boldsymbol{p}, \theta)$, we find

$$p_0(\theta) = \sqrt{\frac{\sqrt{\alpha_{11}^2 - 3\alpha_1\alpha_{111}\dfrac{\theta_{\text{C}} - \theta}{\theta_{\text{C}}}} - \alpha_{11}}{3\alpha_{111}}}. \tag{4}$$

The evolution of the polarization $\boldsymbol{p}$ is generally described by gradient flow kinetics.[50,51,53] Since the latter applies only in the athermal limit (at 0 K), we here model finite temperature via a stochastic extension of the Allen–Cahn equation

$$\mu\dot{\boldsymbol{p}} = -\frac{\partial W}{\partial \boldsymbol{p}} + \nabla \cdot \frac{\partial W}{\partial \nabla \boldsymbol{p}} + \mu\boldsymbol{\eta}, \tag{5}$$

with an inverse mobility $\mu > 0$. $\boldsymbol{\eta}$ represents uncorrelated random noise, which accounts for atomic-level thermal fluctuations at the mesoscale. Under the assumption of thermal equilibrium, the stochastic process $\boldsymbol{\eta}(\boldsymbol{x}, t)$ is identified as a centered Gaussian random variable, which is unbiased and uncorrelated in space and time and whose variance depends on temperature,[47]

$$\langle \boldsymbol{\eta}(\boldsymbol{x}, t), \boldsymbol{\eta}(\boldsymbol{x}', t') \rangle = \frac{2k_{\text{B}}\theta}{\mu V_{\text{char}}\Delta t}\,\delta(t - t')\,\delta(\boldsymbol{x} - \boldsymbol{x}'), \tag{6}$$

where k_{B} denotes Boltzmann's constant, Δt is the numerical time increment, and $V_{\text{char}} = a_{\text{tetr}}^2 c_{\text{tetr}}$ is the volume of a perovskite atomic unit cell (which is assumed to be constant). The effect of temperature, hence, enters the model through (i) the polarization potential and the resulting spontaneous polarization in Eq. (4) and (ii) the thermalized kinetics in Eq. (5). This phase-field model, which was validated against experimental data and shown to produce realistic domain microstructures,[47] is the basis for studying the influence of temperature on DW pinning in porous single-crystalline PZT. Pores are modeled as non-switchable cavities with polarization $\boldsymbol{p} = \boldsymbol{0}$ and vacuum permittivity κ_0.

We solve Eqs. (1), (2), and (5) within a cubic RVE by an FFT-based homogenization scheme[54] with periodic boundary conditions (supplementary material, Sec. II). Experimental conditions of free-standing, electrically loaded samples are realized by enforcing a vanishing average stress, $\langle\boldsymbol{\sigma}\rangle = \boldsymbol{0}$, along with a prescribed average electric field $\langle\boldsymbol{e}\rangle$, representing the applied field. While for small pores relative to the RVE size ($R/L \ll 0.1$), this setup accurately approximates the analytical solution for an isolated pore in an infinite medium (see the supplementary material, Sec. III, including a discussion on numerical accuracy), larger pores ($R/L > 0.1$ at fixed RVE size) model periodic arrays of voids and are viewed representative of porous samples.

Pores in a ferroelectric act as hot spots for domain switching and domain nucleation under an applied electric field, which is amplified to significantly larger local electric fields induced near the pore. This effect becomes apparent in Fig. 1(a), which shows the evolution of the polarization around a spherical cavity of radius $R = 12$ nm and, for improved visibility, 2D results for the polarization p_2/p_0 and the electric field e_2 at 100 K [Figs. 1(b) and 1(c)] and at 300 K [Fig. 1(d)] for comparison. Initially poled with $\boldsymbol{p} = p_0\boldsymbol{e}_2$, symmetric needle-shaped a-domains grow under 45° to compensate for the strain mismatch in the proximity of the pore. The induced electric field above and below the pore favors b^--domains and disfavors the existing b^+-domain. The lowest-energy transition for polarization reversal to occur is by polarization rotation, which corresponds to two subsequent 90°-switching steps, e.g., from a b^+-domain via $a^\pm$-domains to a b^--domain. These newly formed a-domains are a consequence of the induced electric field by the pore and the minimization of the polarization potential $\Psi_{\text{pol.}}$.

In the absence of free charges, the electric field $\boldsymbol{e}^-$ inside the cavity is related to the electric field $\boldsymbol{e}^+$ and polarization $\boldsymbol{p}$ outside the cavity by the jump condition $[\![\boldsymbol{d}]\!] \cdot \boldsymbol{n} = 0$, where $\boldsymbol{n}$ is the outward-pointing surface normal. Inserting Eq. (2) gives the electric field outside the cavity as

$$\boldsymbol{e}^+ = \boldsymbol{e}^- - \frac{1}{\kappa_0}(\boldsymbol{p} \cdot \boldsymbol{n})\boldsymbol{n}, \tag{7}$$

i.e., as a function of the electric field $\boldsymbol{e}^-$ inside the pore and the outside polarization $\boldsymbol{p}$ (whose magnitude is the spontaneous polarization p_0 in the absence of external loads). Since the spontaneous polarization depends on temperature, cf. Eq. (4), the induced electric field also

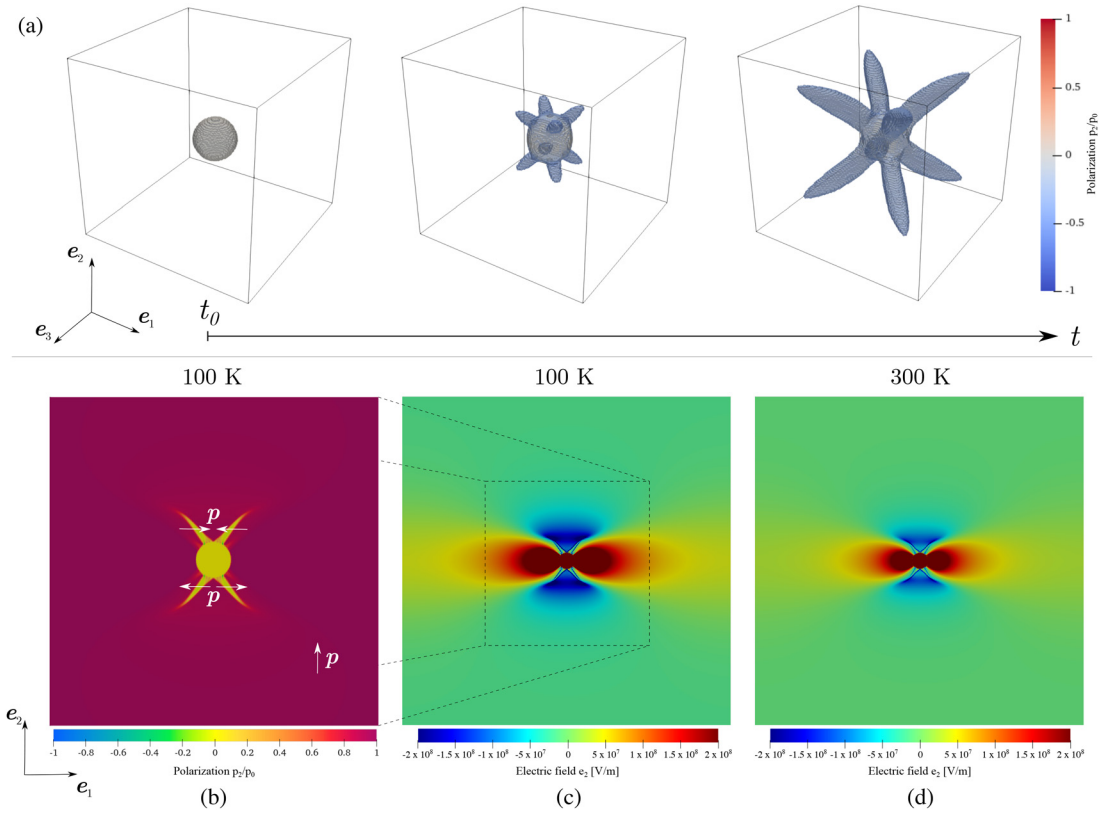

FIG. 1. (a) Snapshots of the 3D polarization evolution ($L = 51$ nm and $\Delta x = a_{\text{tetr}}$), showing regions with a vertical polarization component $\boldsymbol{p}_2(\boldsymbol{x})/p_0 \in [-0.5, 0.5]$ in the vicinity of a spherical cavity with radius $R = 12$ nm for an imposed average field $\langle \boldsymbol{e} \rangle = \boldsymbol{0}$ and average stress-free conditions ($\langle \boldsymbol{\sigma} \rangle = \boldsymbol{0}$). Comparison of the electric field in the vertical direction, $e_2(\boldsymbol{x})$, for an imposed average field $\langle \boldsymbol{e} \rangle = \boldsymbol{0}$ at temperatures $\theta = 100$ and 300 K is shown in (c) and (d), respectively. A zoomed-in version of the region highlighted in (c) visualizes polarization component $p_2(\boldsymbol{x})/p_0$ in (b).

varies with temperature. This is observed when comparing the computed electric field component $e_2(\boldsymbol{x})$ at the two temperatures of 100 and 300 K in Figs. 1(c) and 1(d), respectively. Due to the smaller spontaneous polarization at 300 K, the induced electric field in Fig. 1(d) is lower in amplitude and extends less into the surroundings than at 100 K [shown in Fig. 1(c)]. As a consequence, a decreasing influence of pores onto DW motion with increasing temperature may be expected.

To systematically investigate the influence of pore size and pore separation distance on DWs, we simulate pore–DW interactions in the simpler 2D setting, which gains significant efficiency while not affecting the physics at play (cf. Fig. 1). We consider a 180°-DW interacting with a periodic array of circular pores of equal radii R (simulating a square-shaped RVE of side length $L = \{102, 205, 410\}$ nm with periodic boundary conditions, see Fig. 2). Independent of parameters R and L, the single-crystalline RVE contains initially two ferroelectric domains: the b^+-domain (red) and b^--domain (blue), whose polarizations point up and down, respectively. When applying an average electric field e_2 in the vertical direction, the lower-energy b^+-domain grows by moving the DWs toward the outer boundaries of the RVE. The nonswitchable pores, whose size exceeds the thickness of DWs ($l_0 \approx 0.7$–2 nm Refs. 52 and 55), serve as obstacles to the moving DWs. Their interaction is already apparent before the DW reaches the pore, as shown in Fig. 2(b), where the growing b^+-domain (red) is locally eroded close to the pore by the induced electric field to the left of the cavity. Such erosion of the 180°-DW near defects under an applied field was observed in experiments[21] using near-field scanning optical microscopy. The spreading a^-- and a^+-domains above and below the pore, respectively, connect to the b^+-domain by forming 90°-DWs. Local electric fields in the proximity of the cavity reduce the driving force on the DW, thus slowing down the propagating interface, until it is pinned at the pore [Fig. 2(d)]. Such pinning of an individual DW at an isolated defect,[24] a dislocation,[56] precipitates,[57] secondary phases,[58] a twin[59] and grain[8,60] boundary has been confirmed experimentally. To unpin from the obstacle, the applied electric field must be increased, which in the case of the cavity promotes the following mechanism [Fig. 2(e)]: domains with polarization parallel to the cavity's surface grow, until the top and bottom regions merge to grow a new b$^+$-domain to the right of the pore. This newly formed domain then expands by DW motion and eventually merges with the initial b^+-domain from the center of the RVE [Fig. 2(e) and supplementary material Video 1]. We define the depinning field as the minimum applied electric field required to unpin the DW from the pore(s); it is obtained in simulations by increasing the applied electric field incrementally (with sufficient dwell time between increments, so finite-temperature Brownian motion can show its effect). The

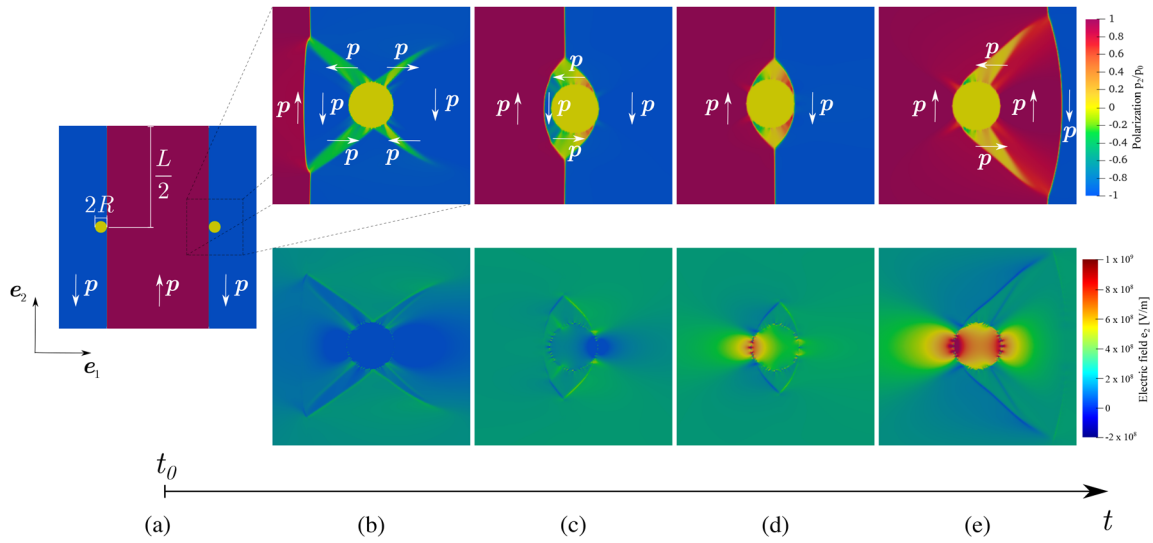

FIG. 2. Snapshots of a simulated ferroelectric DW interacting with a circular cavity, showing polarization component $p_2(\boldsymbol{x}, t)/p_0$ (top row) and electric field component $e_2(\boldsymbol{x}, t)$ (bottom row) at temperature $\theta = 300$ K. (a) The initial configuration includes two ferroelectric domains separated by 180°-DWs with two circular pores of radius R at a distance L, considering periodic boundary conditions. Snapshots (b)–(e) show zoomed-in versions of the highlighted section in (a) for the three cases when (b) and (c) the DW is approaching the void, (d) the DW is pinned by the pore, and (e) the DW unpins from the void. Small arrows indicate the polarization vector directions. For the full simulation, see supplementary material Video 1.

recurring pinning and unpinning of DWs at pores appear as stick-slip behavior of mesoscopic DW motion, or as a pronounced hysteresis at the macroscale.[42]

The impact of pore size (radius R) and pore separation (distance L) on the depinning field is summarized in Figs. 3(a)–3(c) for the three temperatures of $\theta = 200$, 300, 400 K. Overall, the depinning field increases monotonically with pore size, and the slope of the pore-radius-vs-electric-field curve indicates a higher sensitivity of the depinning field to larger pore densities (assuming uniform pore radii). We, hence, conclude that at least two characteristic length-scales are at play: (i) pore radius R determines the locally induced near-field in the vicinity of the void according to Gauss' law, and (ii) distance L between pores accounts for the far-field interference of overlaying electric fields from adjacent pores. To account for these distinct length scales, we define the linear pore density $v_d = 2R/L$ as the ratio of the pore diameter and their distance (which is the domain of influence of a single pore within the ferroelectric). The resulting plot of depinning field vs v_d collapses onto a single master curve $f(v_d)$ at each temperature [Figs. 3(d)–3(f)], each following a linear relation. Note that the phase-field model is valid in the "large-defect" regime, i.e., for large pores with $2R > l_0$, below which a more accurate (atomistic) description is required and where other mechanisms are at play. (The largest DW thickness observed in simulations is about 1 nm at 500 K.)

The interplay of pore size, pore separation distance, and temperature becomes apparent in Figs. 4(a)–4(c), showing the depinning field over a wide temperature range. The effect of temperature is generally dominant over both pore size and concentrations. The pore size gains importance with the decreasing temperature and with the decreasing pore separation distance. When approaching the Curie temperature $\theta_C = 650$ K, the homogeneous disordering of the ferroelectric polarization makes DW motion negligible and significantly reduces the pinning field [seen in the slope $\partial f/\partial v_d$ vs temperature in Fig. 3(g)]. By contrast, in the athermal limit $\theta \to 0$ K, thermal fluctuations are absent, so the associated Brownian motion cannot promote barrier-crossing events in noncoercive regions[47] to lower the depinning field. While for the largest separation distance ($L = 410$ nm), the depinning field depends noticeably on pore size only at low temperatures below 200 K, the effect of pore size is more pronounced at $L = 102$ nm.

Comparing the obtained depinning field at room temperature, $e/e_c \approx 0.044$ (averaged over all radii R at $L = 205$ nm), with hysteresis measurements of PZT-5A,[61,62] reporting $e/e_c = 0.006$, reveals that in reality DW motion is active even below the electric field values reported here; this is expected due to simplifying assumptions and the 2D approximation of a spherical pore, overestimating the local electric field. Despite this difference in the depinning field magnitude, our model captures several key features previously reported from experiments. For example, the nonlinear temperature dependence of the depinning field is in good qualitative agreement with measurements of the DW velocity under random-field pinning in the creep regime[25] in epitaxial PZT films at finite temperature, as shown in Fig. 4(d), where simulated data (normalized by the athermal limit) are compared to experiments.[25] Moreover, the observed stick-slip behavior of DW motion interacting with pores is in agreement with local piezoresponse force spectroscopy measurements that identified the fine structure in the hysteresis loops as a fingerprint of an isolated defect.[24]

In summary, using a temperature-aware phase-field model, we have investigated the pinning of DWs at nano-sized pores in tetragonal PZT under an applied bias field across a wide temperature range. DW pinning strongly affects ferroelectric switching through its impact on DW kinetics. We have highlighted the influence of pore size, pore concentration, and temperature.

Of course, such a model comes with limitations. First, the 2D simplification overestimates the electric field induced by the pore by 50% (supplementary material, Sec. III). In a ferroelectric, we expect

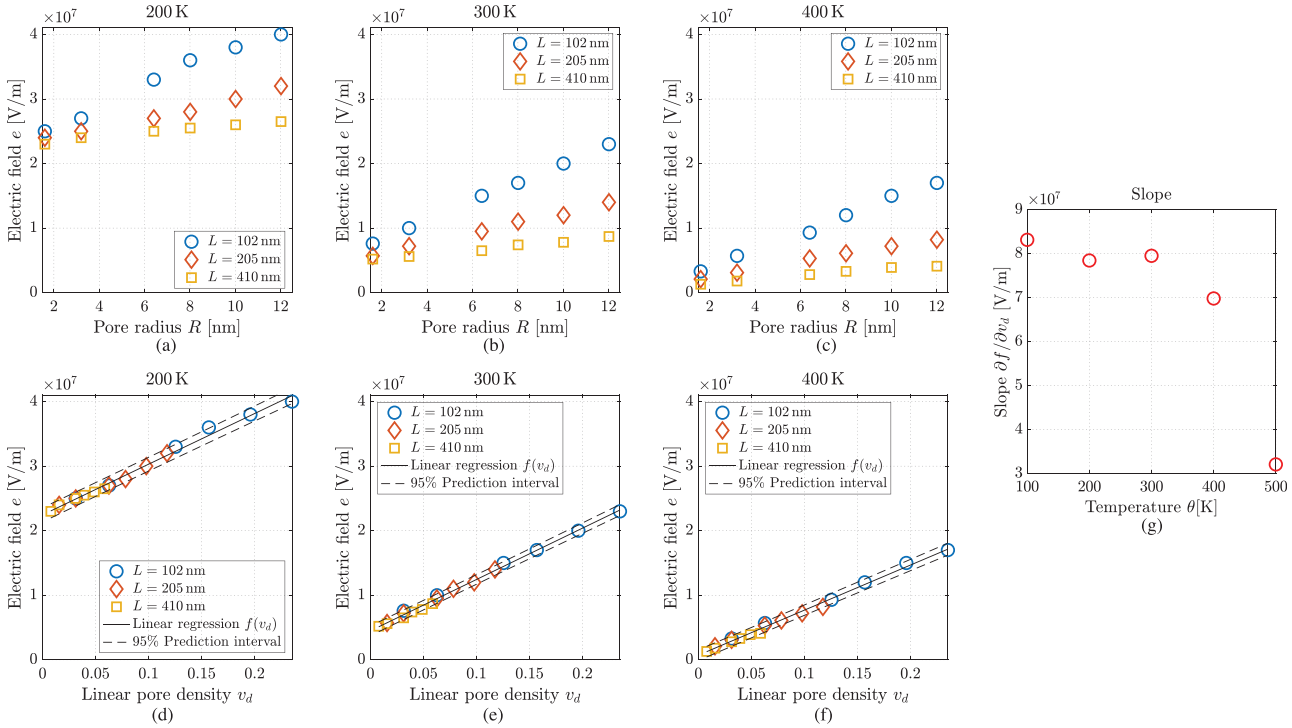

FIG. 3. Influence of the pore radius R (a)–(c) and linear pore density $v_d = 2R/L$ (d)–(f) on the depinning electric field e_2, required for a 180°-DW to unpin from and overcome an array of pores separated at distances $L = \{102, 205, 410\}$nm (line colors) at temperatures $\theta = \{200, 300, 400\}$K (columns). (g) Slope of the depinning field vs v_d for all examined temperatures.

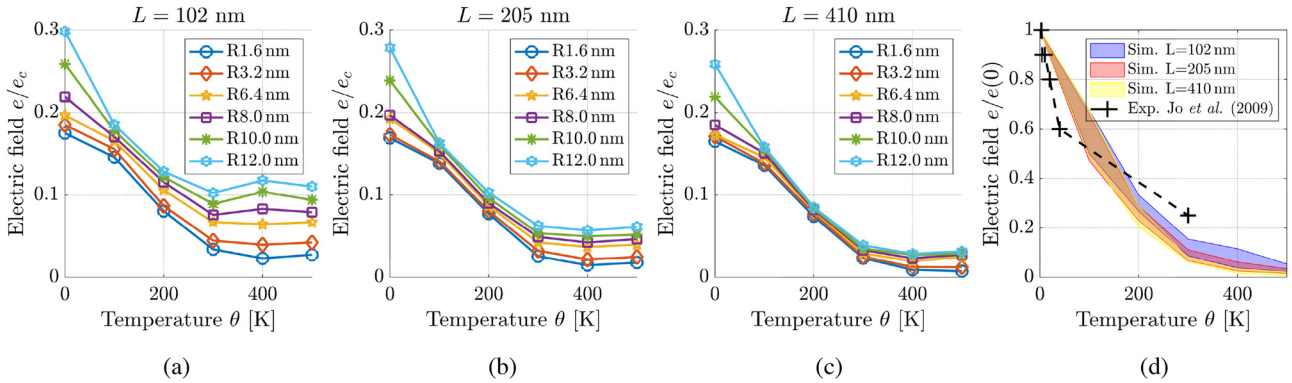

FIG. 4. (a)–(c) Influence of temperature on the electric field e_2 (normalized by the temperature-dependent coercive field e_c) required for a 180°-DW to unpin and overcome an array of pores of radii $R = \{1.6, 3.2, 6.4, 8.0, 10.0, 12.0\}$nm separated by distances $L = \{102, 205, 410\}$nm. (d) Summary of all simulated data [each curve normalized by its athermal value $e(0\ \text{K})$, showing the margin between minimum and maximum field per temperature] in comparison with experimental data.[25]

even smaller depinning fields due to two additional tetragonal variants, which increase the available switching paths and, hence, the probability of thermally induced barrier-crossing events. Second, we focused on 180°-DWs and excluded pinning of initially 90°-DW configurations. Due to the differences in energy barriers, we have observed in analogous studies that 90° depinning fields can be orders of magnitude lower that the ones reported here. However, other physical effects, such as nucleation, are dominant with 90°-DWs and result in a different depinning mechanism, such that a direct transfer of the reported depinning fields to 90°-DW pinning is challenging. Finally, the strain mismatch near pores, which is important for pinning, has not been investigated thoroughly in this study (see the supplementary material Sec. II for a discussion).

Despite these simplifying assumptions, the reported microscale interactions of nano-sized pores with 180°-DWs are in general agreement with experimental observations. For example, the induced

electric field in the proximity of the pore leads locally to polarization reversal, which appears as bending of the DW around the void. This effect has been optically captured and reported as bowing of DWs.[63] Furthermore, we observed a stick-slip behavior of DWs at pores, which is characteristic for the large-defect-regime kinetics[42] and has been verified experimentally on isolated defects,[24] twin boundaries,[59] and dislocations.[56] In addition, theoretical[13] and experimental[64] studies suggest a decrease in the macroscale remanent polarization for higher porosity, which agrees with our findings that more densely packed pores (at constant size) increase microscale DW-pinning. Moreover, the computed temperature dependence of the depinning field shows agreement with measurements of PZT thin films.[25] Our finite-temperature model, hence, reproduces salient features of DW pinning seen in experiments and in agreement with theoretical considerations. It improves the predictability of properties of realistic, porous ferroelectric materials at finite temperature, accounting for DW interactions with dielectric impurities at the microscale for a wide range of the electric field and temperature.

See the supplementary material for the discussion of all material parameters and model details (Sec. I), the computational setup (Sec. II), the benchmark of a single void in an infinite dielectric (Sec. III), and a comparison with PFM measurements (Sec. IV). Supplementary material Video 1 features the DW-pore interaction of Fig. 2.

The authors acknowledge the support from the Swiss National Science Foundation (SNSF) and thank L. Guin and V. Kannan for fruitful discussion.

AUTHOR DECLARATIONS

Conflict of Interest

The authors declare no conflicts of interest.

DATA AVAILABILITY

The data that support the findings of this study are available within the article and its supplementary material.

REFERENCES

[1]J. Curie and P. Curie, "Développement par compression de l'électricité polaire dans les cristaux hémièdres à faces inclinées," Bull. Minéral. **3**, 90–93 (1880).
[2]S. D. Brewster, *Observations on the Pyro-Electricity of Minerals* (William Blackwood, 1824).
[3]G. d Parravano, "Ferroelectric transitions and heterogenous catalysis," J. Chem. Phys. **20**, 342–343 (1952).
[4]P. Bintachitt, S. Jesse, D. Damjanovic, Y. Han, I. M. Reaney, S. Trolier-McKinstry, and S. V. Kalinin, "Collective dynamics underpins Rayleigh behavior in disordered polycrystalline ferroelectrics," Proc. Natl. Acad. Sci. **107**, 7219–7224 (2010).
[5]S. Gorfman, A. A. Bokov, A. Davtyan, M. Reiser, Y. Xie, Z.-G. Ye, A. V. Zozulya, M. Sprung, U. Pietsch, and C. Gutt, "Ferroelectric domain wall dynamics characterized with x-ray photon correlation spectroscopy," Proc. Natl. Acad. Sci. **115**, E6680–E6689 (2018).
[6]N. Bassiri-Gharb, I. Fujii, E. Hong, S. Trolier-McKinstry, D. V. Taylor, and D. Damjanovic, "Domain wall contributions to the properties of piezoelectric thin films," J. Electroceram. **19**, 49–67 (2007).
[7]A. Pramanick, D. Damjanovic, J. E. Daniels, J. C. Nino, and J. L. Jones, "Origins of electro-mechanical coupling in polycrystalline ferroelectrics during subcoercive electrical loading," J. Am. Ceram. Soc. **94**, 293–309 (2011).
[8]D. M. Marincel, H. R. Zhang, J. Britson, A. Belianinov, S. Jesse, S. V. Kalinin, L. Q. Chen, W. M. Rainforth, I. M. Reaney, C. A. Randall, and S. Trolier-McKinstry, "Domain pinning near a single-grain boundary in tetragonal and rhombohedral lead zirconate titanate films," Phys. Rev. B **91**, 134113 (2015).
[9]E. Mercadelli, A. Sanson, and C. Galassi, "Porous piezoelectric ceramics," in *Piezoelectric Ceramics*, edited by E. Suaste-Gomez (IntechOpen, Rijeka, 2010), Chap. 6.
[10]T. Xu and C.-A. Wang, "Grain orientation and domain configuration in 3-1 type porous PZT ceramics with ultrahigh piezoelectric properties," J. Am. Ceram. Soc. **98**, 2700–2702 (2015).
[11]R. L. Johnson-Wilke, R. H. T. Wilke, M. Wallace, A. Rajashekhar, G. Esteves, Z. Merritt, J. L. Jones, and S. Trolier-McKinstry, "Ferroelectric/ferroelastic domain wall motion in dense and porous tetragonal lead zirconate titanate films," IEEE Trans. Ultrason., Ferroelectr., Frequency Control **62**, 46–55 (2015).
[12]T. Zeng, X. Dong, S. Chen, and H. Yang, "Processing and piezoelectric properties of porous PZT ceramics," Ceram. Int. **33**, 395–399 (2007).
[13]R. Khachaturyan, S. Zhukov, J. Schultheiß, C. Galassi, C. Reimuth, J. Koruza, H. von Seggern, and Y. A. Genenko, "Polarization-switching dynamics in bulk ferroelectrics with isometric and oriented anisometric pores," J. Phys. D **50**, 045303 (2017).
[14]D. Skinner, R. Newnham, and L. Cross, "Flexible composite transducers," Mater. Res. Bull. **13**, 599–607 (1978).
[15]J. Schultheiß, J. I. Roscow, and J. Koruza, "Orienting anisometric pores in ferroelectrics: Piezoelectric property engineering through local electric field distributions," Phys. Rev. Mater. **3**, 084408 (2019).
[16]Y. Zhang, M. Xie, J. Roscow, Y. Bao, K. Zhou, D. Zhang, and C. R. Bowen, "Enhanced pyroelectric and piezoelectric properties of PZT with aligned porosity for energy harvesting applications," J. Mater. Chem. A **5**, 6569–6580 (2017).
[17]R. Guo, C.-A. Wang, and A. Yang, "Effects of pore size and orientation on dielectric and piezoelectric properties of 1–3 type porous PZT ceramics," J. Eur. Ceram. Soc. **31**, 605–609 (2011).
[18]K. Carl and K. H. Hardtl, "Electrical after-effects in $Pb(Ti, Zr)O_3$ ceramics," Ferroelectrics **17**, 473–486 (1977).
[19]B. Li, G. Li, Q. Yin, Z. Zhu, A. Ding, and W. Cao, "Pinning and depinning mechanism of defect dipoles in PMnN–PZT ceramics," J. Phys. D **38**, 1107–1111 (2005).
[20]T. Rojac, S. Drnovsek, A. Bencan, B. Malic, and D. Damjanovic, "Role of charged defects on the electrical and electromechanical properties of rhombohedral $Pb(Zr, Ti)o_3$ with oxygen octahedra tilts," Phys. Rev. B **93**, 014102 (2016).
[21]T. J. Yang, V. Gopalan, P. J. Swart, and U. Mohideen, "Direct observation of pinning and bowing of a single ferroelectric domain wall," Phys. Rev. Lett. **82**, 4106–4109 (1999).
[22]T. Tybell, P. Paruch, T. Giamarchi, and J.-M. Triscone, "Domain wall creep in epitaxial ferroelectric $Pb(Zr_{0.2}Ti_{0.8})O\_3$ thin films," Phys. Rev. Lett. **89**, 097601 (2002).
[23]P. Paruch, T. Giamarchi, T. Tybell, and J.-M. Triscone, "Nanoscale studies of domain wall motion in epitaxial ferroelectric thin films," J. Appl. Phys. **100**, 051608 (2006).
[24]S. V. Kalinin, S. Jesse, B. J. Rodriguez, Y. H. Chu, R. Ramesh, E. A. Eliseev, and A. N. Morozovska, "Probing the role of single defects on the thermodynamics of electric-field induced phase transitions," Phys. Rev. Lett. **100**, 155703 (2008).
[25]J. Y. Jo, S. M. Yang, T. Kim, H. N. Lee, J.-G. Yoon, S. Park, Y. Jo, M. Jung, and T. W. Noh, "Nonlinear dynamics of domain-wall propagation in epitaxial ferroelectric thin films," Phys. Rev. Lett. **102**, 045701 (2009).
[26]Y. Xiao and K. Bhattacharya, "A continuum theory of deformable, semiconducting ferroelectrics," Arch. Rational Mech. Anal. **189**, 59–95 (2008).
[27]J. Wang and M. Kamlah, "Three-dimensional finite element modeling of polarization switching in a ferroelectric single domain with an impermeable notch," Smart Mater. Struct. **18**, 104008 (2009).
[28]A. Kontsos and C. M. Landis, "Computational modeling of domain wall interactions with dislocations in ferroelectric crystals," Int. J. Solids Struct. **46**, 1491–1498 (2009).
[29]N. Liu and Y. Su, "The grain-size-dependent behaviors of nano-grained ferroelectric polycrystals: A phase-field study," Acta Mech. **225**, 1335–1345 (2014).
[30]J. J. Wang, P. P. Wu, X. Q. Ma, and L. Q. Chen, "Temperature-pressure phase diagram and ferroelectric properties of $BaTiO_3$ single crystal based on a modified Landau potential," J. Appl. Phys. **108**, 114105 (2010).

[31]P. Fedeli, M. Kamlah, and A. Frangi, "Phase-field modeling of domain evolution in ferroelectric materials in the presence of defects," Smart Mater. Struct. **28**, 035021 (2019).
[32]T. Nattermann, "Interface roughening in systems with quenched random impurities," Europhys. Lett. **4**, 1241–1246 (1987).
[33]T. Nattermann, Y. Shapir, and I. Vilfan, "Interface pinning and dynamics in random systems," Phys. Rev. B **42**, 8577–8586 (1990).
[34]T. Emig and T. Nattermann, "A new disorder-driven roughening transition of charge-density waves and flux-line lattices," Phys. Rev. Lett. **79**, 5090–5093 (1997).
[35]T. Emig and T. Nattermann, "Disorder driven roughening transitions of elastic manifolds and periodic elastic media," Eur. Phys. J. B **8**, 525–546 (1999).
[36]T. Natterman, "Interface phenomenology, dipolar interaction, and the dimensionality dependence of the incommensurate-commensurate transition," J. Phys. C **16**, 4125–4135 (1983).
[37]R. Abeyaratne and J. K. Knowles, "Kinetic relations and the propagation of phase boundaries in solids," Arch. Rational Mech. Anal. **114**, 119–154 (1991).
[38]J. M. Ball, C. Chu, and R. D. James, "Hysteresis during stress-induced variant rearrangement," J. Phys. IV **5**, C8–245 (1995).
[39]K. Bhattacharya, "Phase boundary propagation in a heterogeneous body," Proc. R. Soc. London, Ser. A **455**, 757–766 (1999).
[40]R. D. James, "New materials from theory: Trends in the development of active materials," Int. J. Solids Struct. **37**, 239–250 (2000).
[41]E. K. Salje, "Ferroelastic materials," Annu. Rev. Mater. Res. **42**, 265–283 (2012).
[42]L. Tan and K. Bhattacharya, "Length scales and pinning of interfaces," Philos. Trans. R. Soc. A **374**, 20150167 (2016).
[43]S. M. Ueland and C. A. Schuh, "Grain boundary and triple junction constraints during martensitic transformation in shape memory alloys," J. Appl. Phys. **114**, 053503 (2013).
[44]L. Qiao and R. Radovitzky, "Computational modeling of size-dependent superelasticity of shape memory alloys," J. Mech. Phys. Solids **93**, 93–117 (2016).
[45]A. Savage and R. C. Miller, "Temperature dependence of the velocity of sidewise 180° domain–wall motion in $BaTiO_3$," J. Appl. Phys. **31**, 1546–1549 (1960).
[46]H. L. Stadler and P. J. Zachmanidis, "Temperature dependence of 180° domain wall velocity in $BaTiO_3$," J. Appl. Phys. **35**, 2895–2899 (1964).
[47]R. Indergand, A. Vidyasagar, N. Nadkarni, and D. M. Kochmann, "A phase-field approach to studying the temperature-dependent ferroelectric response of bulk polycrystalline PZT," J. Mech. Phys. Solids **144**, 104098 (2020).
[48]A. Devonshire, "Theory of ferroelectrics," Adv. Phys. **3**, 85–130 (1954).
[49]L. Landau, "On the theory of phase transitions," Zh. Eksp. Teor. Fiz. **7**, 19 (1937) (in Russian), see also http://archive.ujp.bitp.kiev.ua/files/journals/53/si/53SI08p.pdf.
[50]W. Zhang and K. Bhattacharya, "A computational model of ferroelectric domains. Part I: Model formulation and domain switching," Acta Mater. **53**, 185–198 (2005).
[51]Y. Su and C. M. Landis, "Continuum thermodynamics of ferroelectric domain evolution: Theory, finite element implementation, and application to domain wall pinning," J. Mech. Phys. Solids **55**, 280–305 (2007).
[52]B. Völker, P. Marton, C. Elsässer, and M. Kamlah, "Multiscale modeling for ferroelectric materials: A transition from the atomic level to phase-field modeling," Continuum Mech. Thermodyn. **23**, 435–451 (2011).
[53]L. Q. Chen, "Phase-field method of phase transitions/domain structures in ferroelectric thin films: A review," J. Am. Ceram. Soc. **91**, 1835–1844 (2008).
[54]A. Vidyasagar, W. Tan, and D. Kochmann, "Predicting the effective response of bulk polycrystalline ferroelectric ceramics via improved spectral phase field methods," J. Mech. Phys. Solids **106**, 133–151 (2017).
[55]Y. Cho, K. Matsuura, N. Valanoor, and R. Ramesh, "Direct domain wall thickness measurement using scanning nonlinear dielectric microscopy," Ferroelectrics **292**, 171–180 (2003).
[56]P. Gao, C. T. Nelson, J. R. Jokisaari, S.-H. Baek, C. W. Bark, Y. Zhang, E. Wang, D. G. Schlom, C.-B. Eom, and X. Pan, "Revealing the role of defects in ferroelectric switching with atomic resolution," Nat. Commun. **2**, 591 (2011).
[57]C. Zhao, S. Gao, T. Yang, M. Scherer, J. Schultheiß, D. Meier, X. Tan, H.-J. Kleebe, L.-Q. Chen, J. Koruza, and J. Rödel, "Precipitation hardening in ferroelectric ceramics," Adv. Mater. **33**, 2102421 (2021).
[58]L. M. Riemer, K. Lalitha, X. Jiang, N. Liu, C. Dietz, R. W. Stark, P. B. Groszewicz, G. Buntkowsky, J. Chen, S.-T. Zhang, J. Rödel, and J. Koruza, "Stress-induced phase transition in lead-free relaxor ferroelectric composites," Acta Mater. **136**, 271–280 (2017).
[59]S. Jesse, B. J. Rodriguez, S. Choudhury, A. P. Baddorf, I. Vrejoiu, D. Hesse, M. Alexe, E. A. Eliseev, A. N. Morozovska, J. Zhang, L.-Q. Chen, and S. V. Kalinin, "Direct imaging of the spatial and energy distribution of nucleation centres in ferroelectric materials," Nat. Mater. **7**, 209–215 (2008).
[60]D. M. Marincel, H. Zhang, S. Jesse, A. Belianinov, M. B. Okatan, S. V. Kalinin, W. M. Rainforth, I. M. Reaney, C. A. Randall, and S. Trolier-McKinstry, "Domain wall motion across various grain boundaries in ferroelectric thin films," J. Am. Ceram. Soc. **98**, 1848–1857 (2015).
[61]M. W. Hooker, "Properties of PZT-based piezoelectric ceramics between-150 and 250 °C," Technical Report No. NASA/CR-1998-208708 (NASA, 1998).
[62]W. L. Tan, K. T. Faber, and D. M. Kochmann, "In-situ observation of evolving microstructural damage and associated effective electro-mechanical properties of PZT during bipolar electrical fatigue," Acta Mater. **164**, 704–713 (2019).
[63]J. Yang, *An Introduction to the Theory of Piezoelectricity, Advances in Mechanics and Mathematics* (Springer US, 2006).
[64]Y. Zhang, J. Roscow, R. Lewis, H. Khanbareh, V. Y. Topolov, M. Xie, and C. R. Bowen, "Understanding the effect of porosity on the polarisation-field response of ferroelectric materials," Acta Mater. **154**, 100–112 (2018).